Upwelling Radiance at 976 nm Measured from Space Using a CCD Camera

Abhijit Biswas[1], Joseph M. Kovalik, Bogdan Oaida, Matthew J. Abrahamson and Malcolm W. Wright
Jet Propulsion Laboratory, California Institute of Technology, 4800 Oak Grove Dive, Pasadena, CA 91109.

ABSTRACT

The Optical Payload for Lasercomm Science (OPALS) Flight System on-board the International Space Station uses a charge coupled device (CCD) camera for receiving a beacon laser from Earth. Relative measurements of the background contributed by upwelling radiance under diverse illumination conditions and varying terrain is presented. In some cases clouds in the field-of-view allowed a comparison of terrestrial and cloud-top upwelling radiance. In this paper we will report these measurements and examine the extent of agreement with atmospheric model predictions

Keywords: Upwelling radiance, 976 nm, CCD Camera

1. INTRODUCTION

Free-space optical communications and other space- and air-borne applications involving the detection of a ground transmitted laser are vulnerable to additive background noise contributed by upwelling radiance (UR) from the sun-illuminated Earth surface, under daytime conditions. The noise sensed depends on a number of factors related to the nadir pointing receiver design and Earth-Sun geometry. Among the latter are: (i) the angle between the space-to-ground line-of-sight and solar azimuth relative to the observer's viewing direction, (ii) surface terrain or cloud deck albedo variations, and (iii) atmospheric attenuation including the presence of clouds, aerosols, water vapor all of which absorb and scatter sunlight; and (iv) surface artifacts that cause "glint" due to transient specular reflections that can overwhelm the laser signal. Among receiver design parameters are: (i) detector field-of-view, (ii) detector spectral responsivity, (iii) the spectral noise-equivalent bandwidth of optical filters in the detector path.

In this paper we present experimental measurements of UR made by the Optical PAyload for Lasercomm Science (OPALS)[1] on-board the International Space Station (ISS). The OPALS Flight System (FS) uses a commercial silicon CCD camera with a 2.2 cm aperture diameter lens and a wide field-of view (FOV) of 7 × 8 degrees. A spectral filter centered at approximately 976 nm with a full-width half maximum of approximately 8nm is mounted in front of the lens. A 976 nm laser that serves as a continuous wave (cw) beacon is transmitted from the ground station. The results discussed in this paper are for flights over the OPALS primary ground station (GS) which utilized the Optical Communication Telescope Laboratory (OCTL)[2] located at Table Mountain near Wrightwood, CA (North latitude 34.4° and West longitude 117.7°).

We compare UR predictions using MODTRAN[3] with OPALS measurements. The comparison is intended to serve as an initial evaluation of the effectiveness with which atmospheric model assumptions can guide the design of optical communications and other similar system designs. These studies may eventually reduce the uncertainty in making atmospheric model assumptions which often lead to overly conservative choices that drive system costs. It is worth noting that the 976 nm wavelength band lies on the edge of a broad atmospheric water vapor absorption feature centered at 944 nm. However, no independent measurements of water vapor content are available for any sort of correlation.

The layout of the remainder of the paper is as follows. Section 2 describes the terrain and its variations encountered during OPALS measurements and the corresponding MODTRAN predictions of UR. Section 3 will present the inferred

[1] Abhijit.Biswas@jl.nasa.gov; phone (818)-354-2415; fax (818)-393-6142;
© 2015 California Institute of Technology. Government sponsorship acknowledged

UR from the OPALS CCD camera measurements recorded when these geometries were encountered. In Section 4 a comparison of measurements with predictions will be discussed followed by concluding remarks in Section 5.

2. OPALS CONFIGURATION FOR UPWELLING RADIANCE

2.1 ISS Overflights and Terrain

Figure 1 shows two Google Map views of OCTL at different zoom levels. The scaling of these views do not correspond to the images recorded by the OPALS camera on-board ISS but are presented as an aid to visualizing the terrain from which UR is sensed. Figure 1a corresponds to a ISS zenith view (approximately 400 km range) while Figure 1b represents a view from a slant range of about 1300 km.

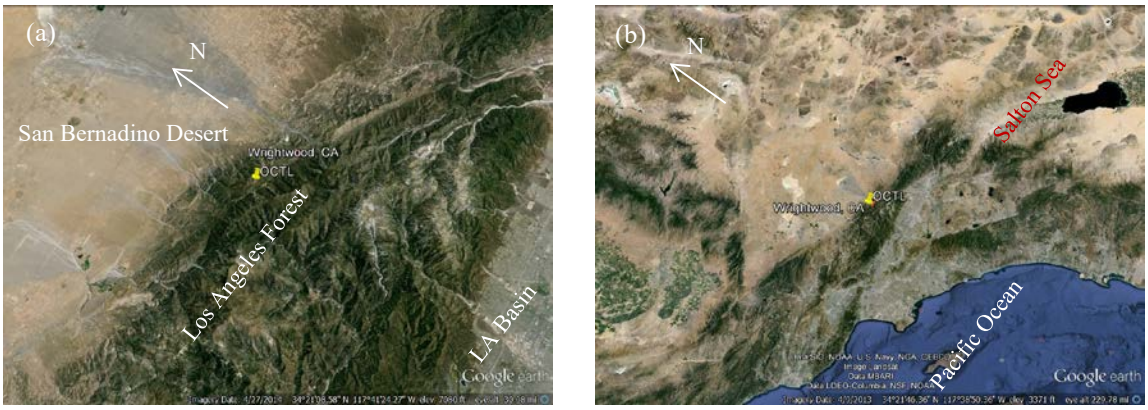

Figure 1. Google Earth images showing terrain around OCTL (a) 400 km zenith view and (b) 1300 km slant range view

Figure 1a shows OCTL located at the edge of the Los Angeles National Forest with mountains covered by forest to the south extending into the Los Angeles basin. To the north is the flat San Bernadino desert. In Figure 1b the longer path slant range view displays a more diverse terrain with a portion of the ocean and the Salton Sea also in view. In addition to the diversity of the terrain the ground area imaged on a camera pixel is changes continuously as does the relative angle between the viewing line-of-sight (LOS) and the solar azimuth angle. The dynamic surface albedo variations sampled during an overflight are complex and difficult to model with confidence. An initial comparison is nonetheless made in this report using simple assumptions. Some of the roads and mountain trails discernible in Figure 1a are examples of artifacts that can contribute to "glint" due to transient specular reflection under certain solar illumination geometries. These situations were encountered during the OPALS demonstration and are reported[4] in a companion paper in this volume.

The forest terrain altitude above to sea level (ASL) is an average of 2 km whereas for the desert terrain mean altitude is about 1 km. The ocean and water is at sea level and cloud-deck is assumed to be at 3.5 km though sub-visual-cirrus is assumed to be as high as 10 km.

2.2 UR Assumptions

MODTRAN UR estimates were made assuming a 1976 standard US atmosphere. Slant path radiance with scattering assumed multiple scattering flux at the observer. MODTRAN default altitude profiles for temperature, pressure, water vapor, ozone, methane, nitrous oxide and carbon monoxide were used. For speed of computation the Modtran 2 multiple scattering model was used. Surface albedo options built into MODTRAN were used, namely, forest, desert, ocean and cloud deck. Two aerosol models were examined: (i) rural visibility of 23 km with no clouds or rain; (ii) rural visibility 5 km with sub-visual cirrus clouds at 10 km height and 1 km thick.

The scattering geometry assumed an observer at the top of the atmosphere (100 km) with the altitudes of the upwelling surface chosen from Section 2.1. Figure 2 shows the geometry used for MODTRAN calculations.

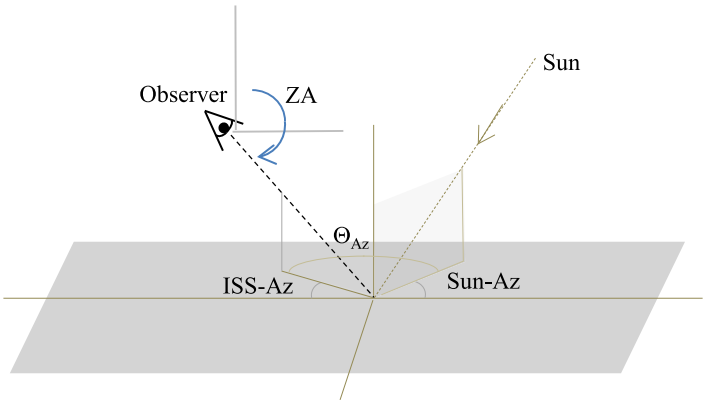

Figure 2. Geometry used for MODTRAN UR where Θ_{Az} represents the azimuth angle difference between the ISS and the Sun position while ZA represents the observer zenith angle which ranges from approximately 100 – 178 degrees.

The ISS azimuth and elevation changed continuously, whereas the Sun position remained nearly constant over the 100-200 second OPALS line-of-sight duration for OCTL overflights.

In this report we analyze two OPALS passes. For these passes UR was estimated for a few combinations of observer zenith angle (ZA), and the sun azimuth angle (Θ_{Az}) (see Figure2). The Sun zenith angle and day of year for the pass were also input to the model. Daytime passes on July 22, 2014 and July15, 2014 were used.

2.3 Upwelling Radiance Estimation

For the two passes Figure 3 shows the variation of ZA and Θ_{Az} based on recorded telemetry of the FS and GS gimbal positions and the sun position at the time of the pass.

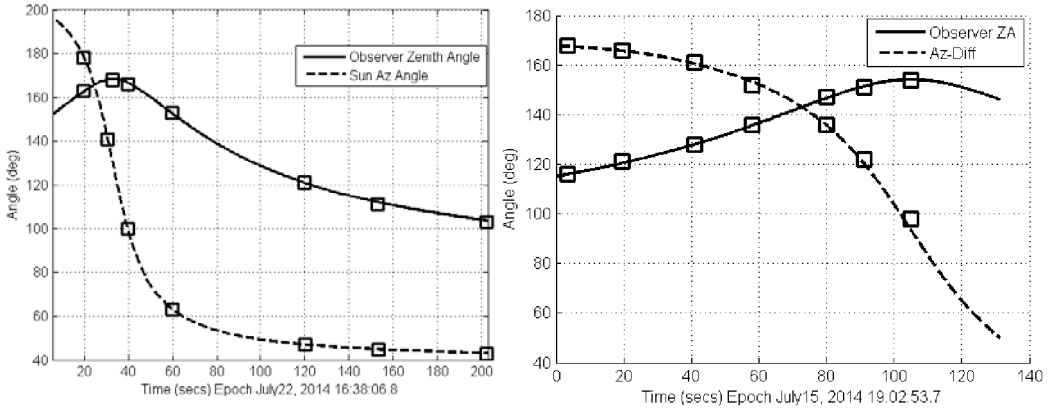

(a) (b)

Figure 3. Variation ZA and relative sun azimuth Θ_{Az} for (a) July22, 2014 and (b) July 15, 2014 passes. The squares represent the pair of ZA values at which the UR was computed.

The squares placed on the lines which appear in pairs were used to compute UR predicted by MODTRAN for the pass geometries under the assumptions summarized in Section 2.2. ZA and Θ_{Az} plotted in Figure 3 were for durations during which the line-of-sight between the FS and GS was "locked" as described in the closed loop operations[4]. The laser beacon[5] transmitted from OCTL was maintained in the center of the OPALS FS camera FOV.

Figure 4 shows the UR for desert and forest albedos each shown with the two aerosol models listed in Section 2.2, namely the 23 km rural visibility model with no clouds or rain and the 5-km visibility model with sub-visual cirrus. Θ_{Az} gets smaller starting at 178-deg and decreasing to 43-deg. The dashed vertical line shows the center wavelength (CWL) of the spectral filter used by OPALS. Note that the center wavelength of the OPALS spectral filter coincides with the edge of a strong water vapor absorption band centered at 940 nm. The observer zenith angle increases i.e. the ISS zenith angle also increases. This link was acquired with the ISS close to zenith (see Figure 3) reaches peak at about 80°

(approx. 170° ZA as defined in Figure 2) and then decreases to about 102°. These passes that are acquired near zenith are infrequent and were encountered twice during OPALS operations when the ISS was in a special docking configuration.

For both forest and desert albedos with 23 km visibility the first 4 pairs of ZA and Θ_{Az} do not change the UR as shown by the spectral plots in two left panels of Figure 4. The last three ZA and Θ_{Az} show a more appreicable increase in UR. For the first 4-points the air-mass (or ISS zenith angle) change is relatively small though Θ_{Az} changes by more than 120-deg. For the last 3 points the Sun azimuth does not change much but the air-mass changes significantly. The difference in radiance due forest and desert albedo cannot be made out from the plots though close examination show the forest to be slightly higher.

Changing the aerosol model to 5 km visibility is shown in the right panels of Figure 4. Here just the two starting and ending pair of ZA and Θ_{Az} were analyzed. Slightly different behavior is exhibited by the desert and forest albedos. While the 5 km visibility results in overall increase in UR for the two extremes of pass geometry, the desert case shows a relatively smaller difference between the starting and ending ZA and Θ_{Az} combination. Furthermore, the smaller ZA and Θ_{Az} combination yields a higher overall radiance in contrast to what is observed for any of the other cases shown.

In many but not all the plots in Figure 4 there is broad dip that around 0.6 micrometers that we offer no explanation for except to point out that it is close to the peak of the solar emission spectrum.

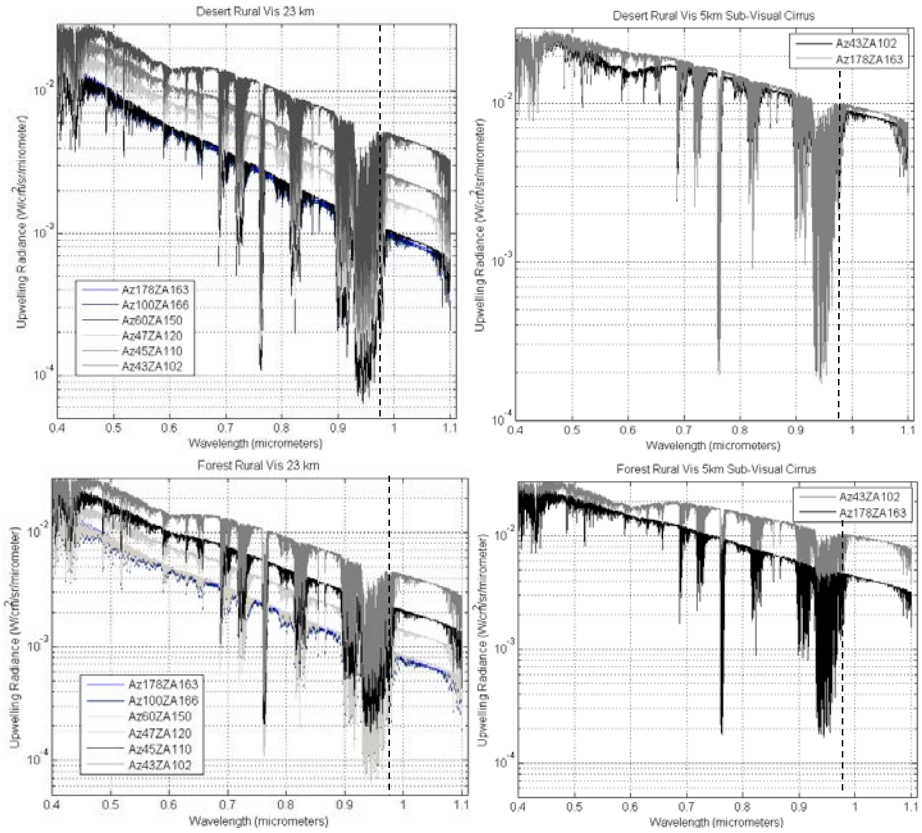

Figure 4. July 22, 2014 pass UR computed with for the two aerosol models listed in Section 2.2 for forest and desert albedo.

For comparison Figure 5 shows some computations for ocean albedo for the July 22, 2014 pass. The overall decrease in UR in the near-infrared is noteworthy, specifically < 2E-3 W/cm^2/sr/μm for ocean compared to 5E-3 W/cm^2/sr/μm for forest

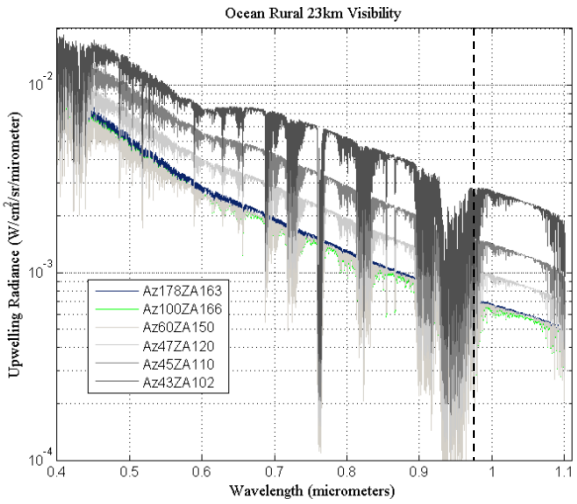

Figure 5. Spectral radiance computed for Ocean albedo using rural 23 km visibility aerosol model.

Figure 6 shows the UR computed for the July 15 pass. Here only desert was analyzed for the two aerosol models using ZA and Θ_{Az} shown in Figure 3b. Though UR increases with decreasing Θ_{Az} and ZA (increasing airmass) the differences are small and hard to discern from Figure 5.

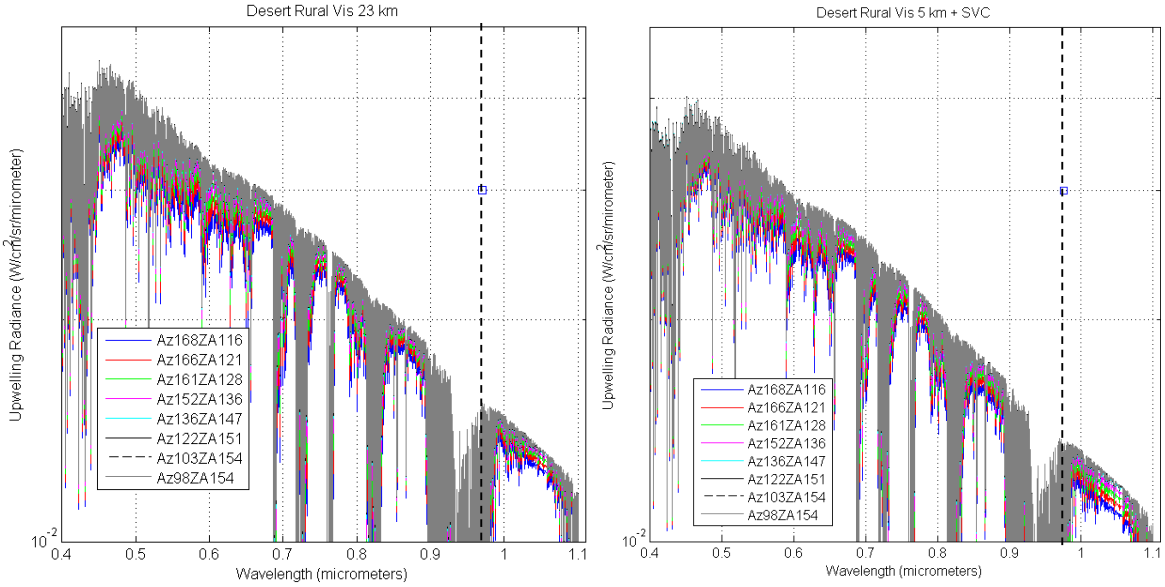

Figure 6. Spectral radiance computed for Desert albedo using rural 23 km and 5 km visibility aerosol models.

Finally in Figure 7 computations for cloud-deck albedo with clouds approximately 3.5 km above ASL are shown for both aerosol models. Interestingly enough for 23 km visibility the UR trend Θ_{Az} and ZA for most of the terrain cases is reversed here with much lower UR values. On the other hand changing to a 5 km visibility model indicates a significant increase in UR, close to an order of magnitude around 976 nm; and the dependence on Θ_{Az} and ZA observed for the surface terrain is restored.

A quick recap of the UR computations using a combination of Θ_{Az} and ZA encountered during two OPALS passes indicates higher UR when both Sun azimuth and air-mass decrease. However, some exceptions to this trend were also pointed out. A more comprehensive explanation of these exceptions and the data itself is beyond the scope of the present work. We will move on to comparing these predictions with camera measurements

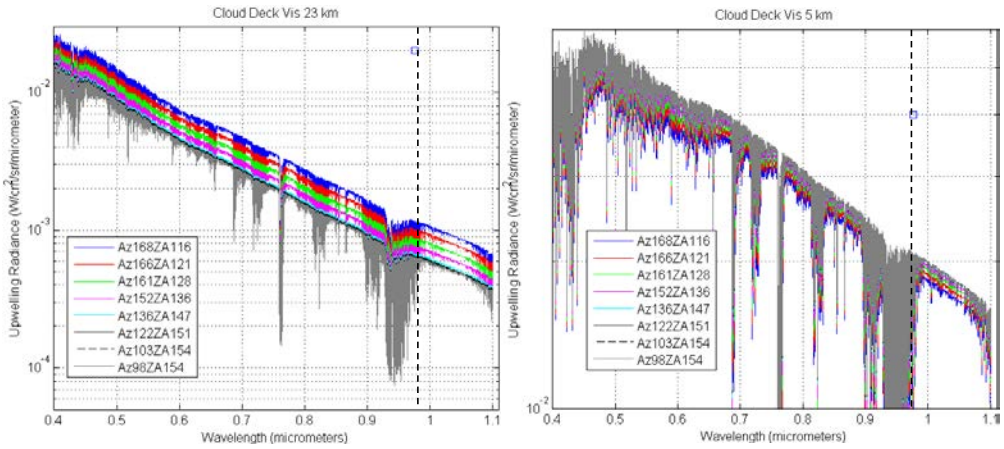

Figure 7. Spectral radiance computed for cloud deck albedo using rural 23 km and 5 km visibility aerosol models.

A noteworthy feature of the spectral radiance for all the albedos considered is the nearly order of magnitude stronger radiance at around 0.5 micrometers. At this wavelength the silicon CCD camera responsivity is significantly higher than at the beacon wavelength of 976 nm so that insufficient blocking by the spectral filter may result in non-negligible out of band leakage. The filter function provided by the manufacturer was multiplied by radiance shown and the camera quantum efficiency curve in order to evaluate this effect. The resulting function multiplied by the fixed collection area of the camera (2.2 cm diameter) and fixed pixel solid angle (~ 69E-9 steradians) to obtain a W/cm^{-1} versus cm^{-1} plot. By integrating this function over the filter in-band frequency region and comparing to the integral over the out-band region the out-of-band leakage is estimated at less than 3%. The W/cm^{-1} can be converted into photons/sec/cm^{-1} and multiplied by the integration and camera gain to provide photo-electrons vs frequency. An example of such a plot is shown in Figure 8 where the Desert terrain with 23-km visibility and no clouds or rain was used. The first combinations of sun-azimuth (AZ) and observer zenith angle (ZA) are very closely overlapped while the last three functions (Az47ZA120, Az45, ZA110 and Az43ZA102) show discernible increased background flux.

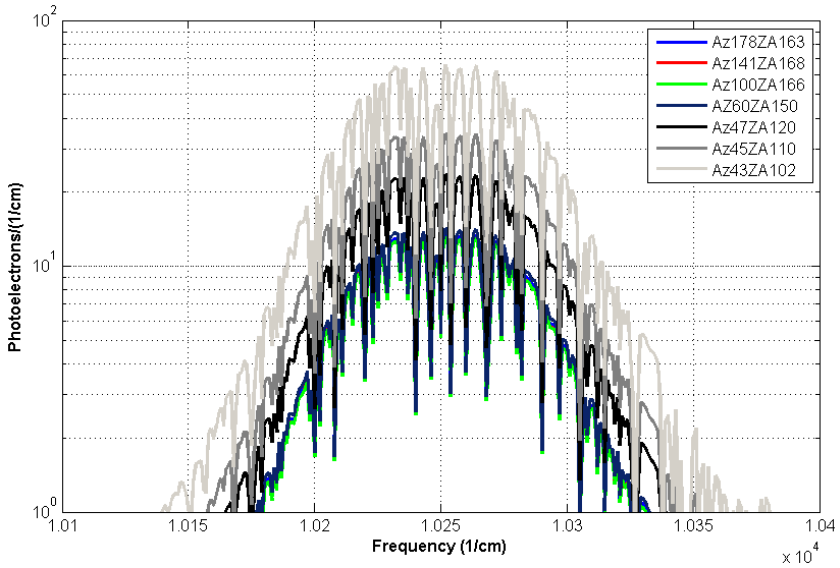

Figure 8. In-band photo-electrons per pixel for Desert terrain with 23-km visibility and no clouds or rain obtained by converting upwelling radiance frequency function with filter transmission, camera responsivity, integration time and camera gain.

The structure shown in the function is attributed to the water vapor absorption features as resolved by MODTRAN since the frequency band is on the wing of the broad water vapor absorption centered at 940 nm.

3. OPALS CAMERA MEASUREMENTS

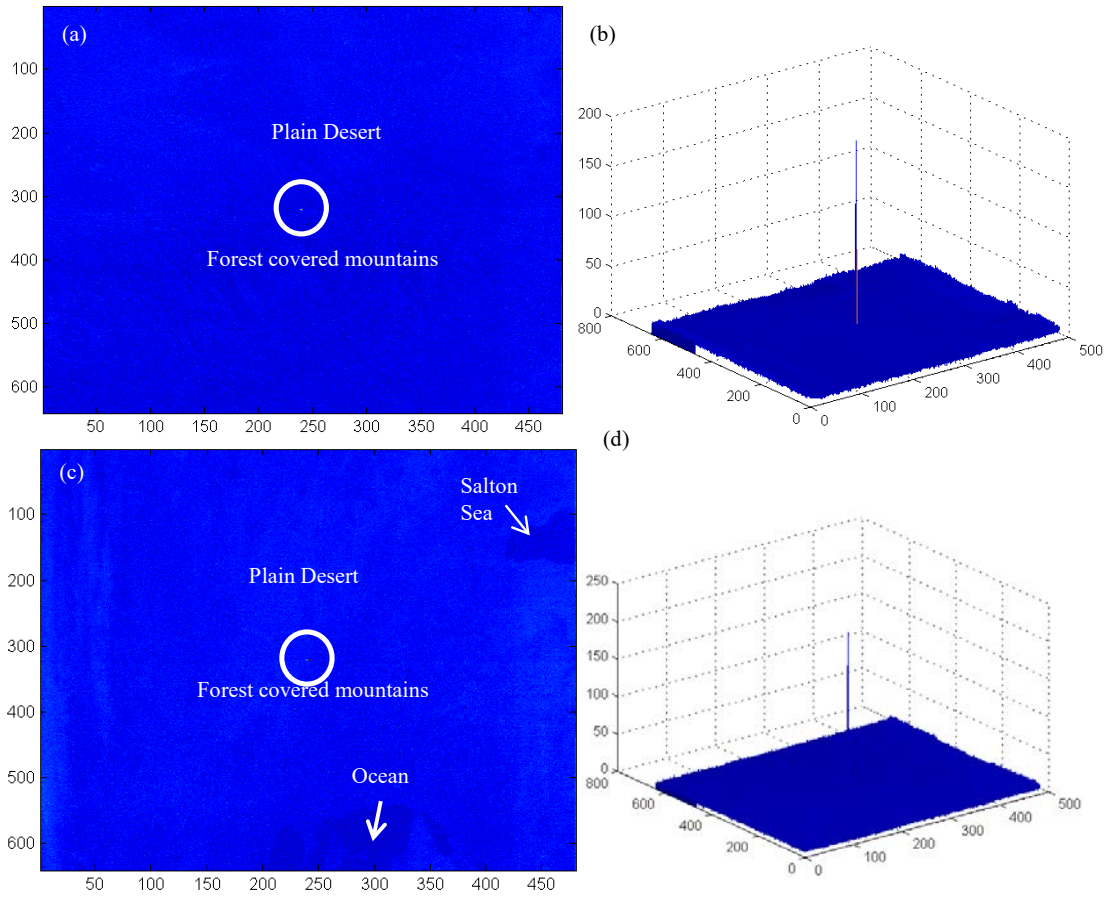

Figure 9. July22, 2014 (a) 16:38:14.2 UTC start of pass, beacon laser spot centered in circle, mountains (average alt. ~2 km) and forest lower half, desert floor (average alt ~1 km) upper half; (b) 3-d mesh showing beacon; (c) 16:41:24.8 UTC end of pass, with ocean and Salton sea imaged from slant range of 1300 km; (d) mesh image of c showing the beacon.

Figure 9 shows frames recorded on July 22, 2014. Figure 9a was early in the pass after beacon acquisition close-loop "lock" while Figure 9c is toward the end of the pass just prior to loss of "beacon lock". Three-dimensional mesh plots (Figure 9b and 9d) show a clearer representation of the relatively bright beacon spot. The near overhead view in Figure 9a is similar to Figure 2a with the mountains covered by forest on bottom half of the image and desert floor on the upper half of Figure 9a. Figure 9c is closer to Figure 2b.

On July 15 the pass was acquired at a low elevation of about 26° and then reaches a peak value of 56° at which point cloud attenuation caused intermittent link drop-outs. Figure 10 shows a camera frame from early (Figure 10a) and late (Figure 10c) in the pass. Once again Figure 10b and 10d show the beacon in a three-dimensional mesh plot. Only the portion of the pass over which beacon lock was maintained was analyzed with a brief link interruption due to cloud line-of-sight blockage.

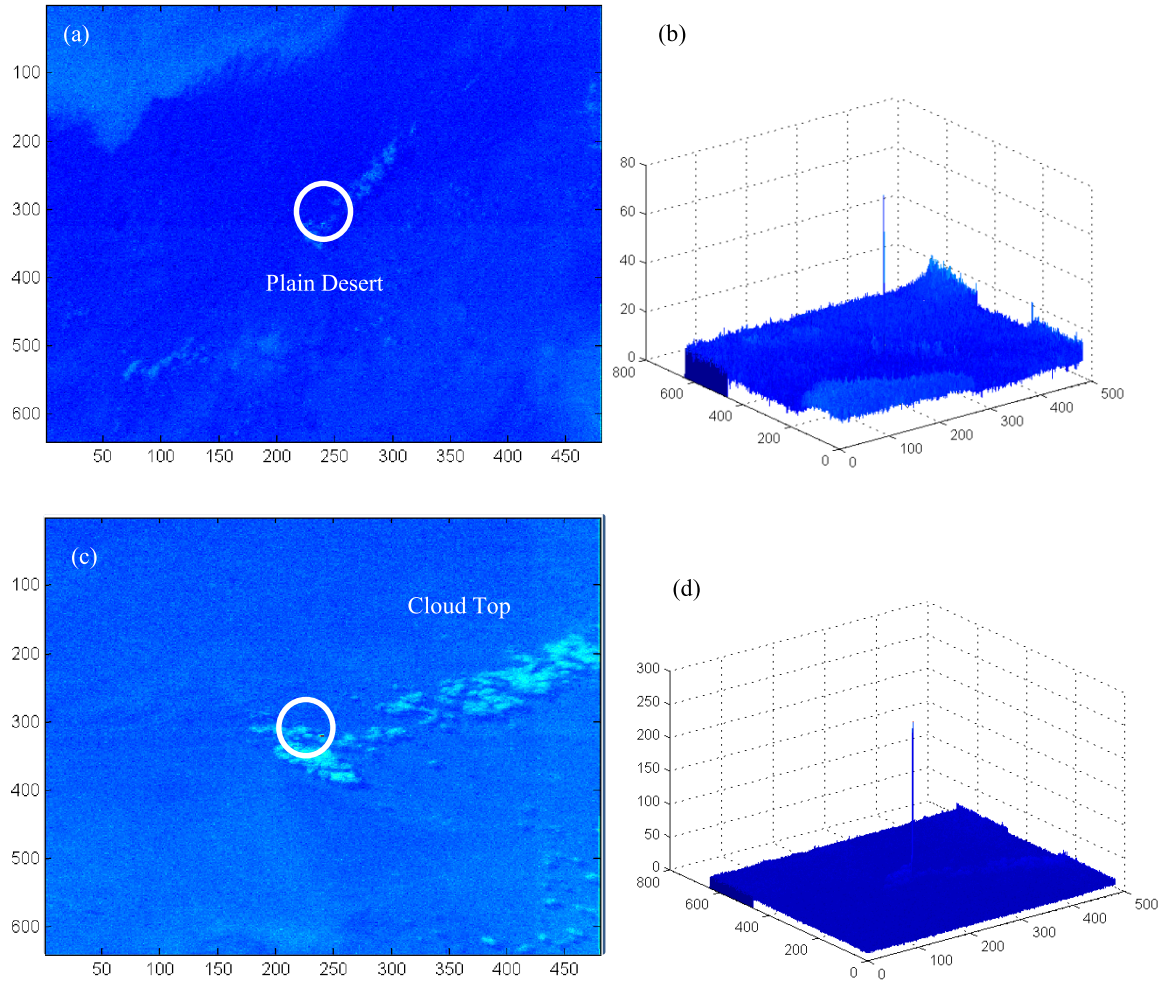

Figure 10. July15, 2014 (a) 19:02:46.7 UTC start of pass, beacon laser spot centered in circle with slant range of ~ 800 km with partially cloudy conditions; (b) 3-d mesh of image (a) showing beacon; (c) 19:04:31.2 UTC near end of pass with ISS at ~ 450 km overlooking partial cloud deck ; (d) mesh of image (c) showing the beacon.

4. COMAPRISON OF MEASURED VERSUS ESTIMATED BACKGROUND

4.1 July22 2014 Pass

30 × 30 pixel regions of the recorded camera frames on July 22 were selected to correspond to desert and Forest covering mountain terrain. The results of this time series are compared with the time series of the estimated background calculated from upwelling radiance. Figure 11 shows this plot where the derived photoelectrons per pixel have been converted to camera digital number using the full well capacity of the pixels and 8-bit resolution. The absolute count numbers are quite different with a factor of 10 lower in the early pass versus a factor of 4 less late in the pass. Uncertainties in camera gain characteristics and responsivity make an absolute comparison of counts somewhat unreliable. The desert calculations show higher counts than the forest for one of the regions (solid lines) but nearly comparable for the regions represented by (dashed lines). The overall trend of increasing background with time into the pass show qualitative agreement but the characteristics of the increase are quite different. The calculations suggest a monotonic increase whereas the measurements flatten out and even hint at a slight decrease. The comparison shows significant deviation between calculations and measurements and if the calculations were relied upon for designing the system background would be much higher than predicted. The measured background likely includes stray light

scattering and reflecting from the ISS structure which is not accounted for in the calculations. The variations in terrain surface albedo are also not accounted in MODTRAN. The comparison presented is an initial attempt at reconciling theoretical models with measurements and needs further study, however, and approach based on testing with background emulation rather than relying on theoretical models is also implicit. For the OPALS system no calibrated testing with background light was performed.

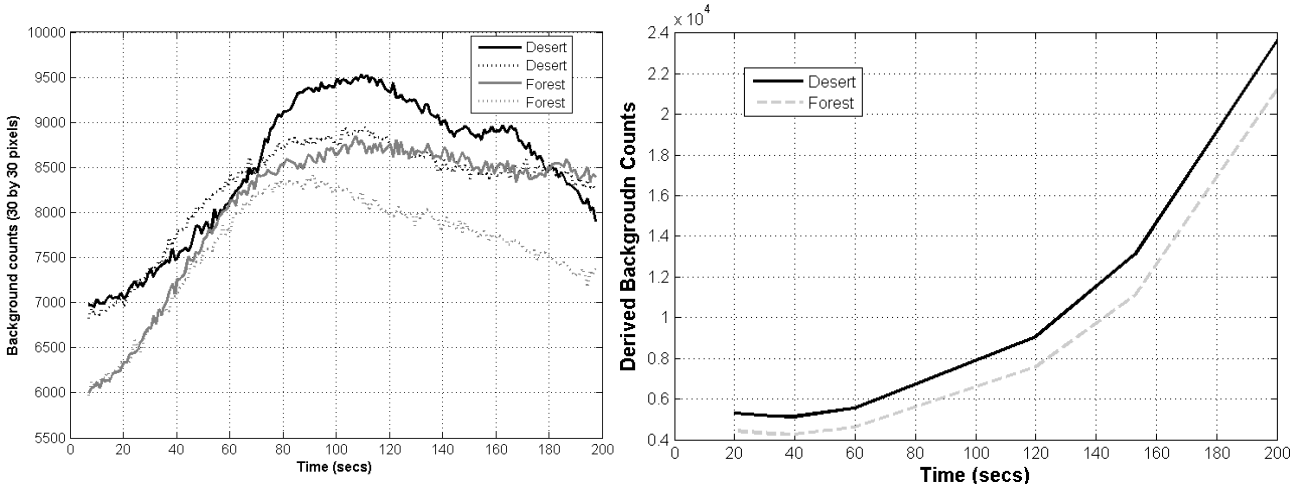

Figure 11. The right panel shows measured background from desert and forest terrain and the right panel shows calculated photoelectrons per pixel.

Figure 12 shows a comparison between the Desert and Forest terrain with ocean

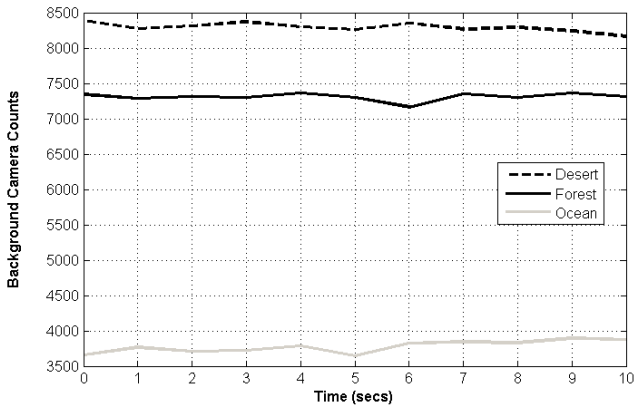

Figure 12 Comparing background counts from ocean with desert and forest terrain.

Note that the factor of 2 reduction in upwelling radiance predicted by theory is supported by the measurements shown in Figure 12. The data was from a few seconds toward the end of the pass when the ocean was in the camera view.

4.2 July 15, 2014

Figure 13 shows a comparison of the measured and derived camera counts for the July 15 pass. In this case the derived counts are higher than the measurement. The fact that the measured cloud top measurements cross over the Desert floor measurements can be explained by the larger area imaged at a distant slant range at the beginning of the pass that combined desert and cloud terrain whereas at the later time in the pass only cloud was imaged. Once again there is qualitative agreement in that both measurements and predictions indicate an increase in background, however, the rates of increase in background do not match.

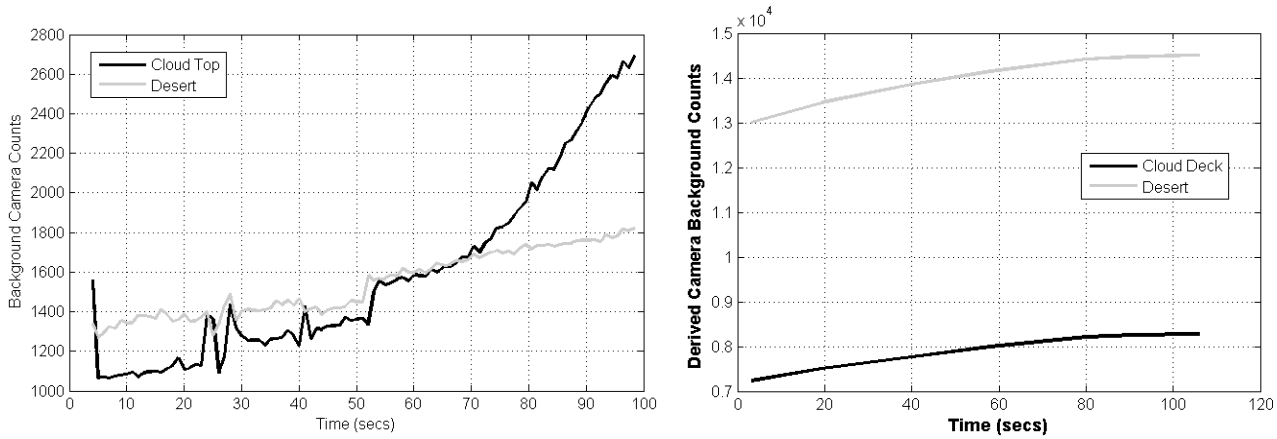

Figure 13. Measured (left panel) and derived (right panel) background from desert and cloud deck for a rural visibility 5 km with sub-visual cirrus aerosol model are compared.

5. CONCLUSIONS

In this report initial comparison of daytime background counts made by a CCD camera on the OPALS FS on-board the ISS are made with predictions made using MODTRAN. Making these comparisons is difficult and fraught by uncertainty in model parameters and assumptions. As expected the models assume idealized uniform surface albedos whereas the terrain imaged in the camera shows surface variations in albedo and altitude. No hard conclusions can be drawn from comparison presented. Qualitative agreement of relative background contributions from surfaces with different albedos is consistent. Further study and analysis of more data is needed to make the results here statistically significant. The need for calibrating camera and sensors for background as well as signal is also important for better understanding the background noise effects.

ACKNOWLEDGEMENTS

The authors would like to thank all members of the OPALS team present and past for their dedication and efforts which made the measurements reported here possible. The work described was carried out at the Jet Propulsion Laboratory (JPL), California Institute of Technology under contract with the National Aeronautics and Space Administration (NASA).

REFERENCES

[1] Oaida, Bogdan V., Wu, W., Erkmen, Baris I., Biswas, A., Andrews, Kenneth S., Kokorowski, M., Wilkerson, M., "Optical link design and validation testing of the Optical Payload for Lasercomm Science (OPALS) system," Proc. SPIE 8971, 89710U-1-15, (2014).

[2] Wilson, K.E., Page, N., Wu, J., Srinivasan, M., "The JPL Optical Communications Telescope Laboratory Test Bed for the Future Optical Deep Space Network," Inter-Planetary Network (IPN) Progress Report, May 15, 2003, http://tmo.jpl.nasa.gov/progress_report/42-153/153G.pdf.

[3] Berk, A., Bernstein, L. S., Anderson, G. P., Acharya, P. K., Robertson, D. C., Chetwynd, J. H., Adler-Golden, S. M., "MODTRAN Cloud and Multiple Scattering Upgrades and Application to AVIRIS," Remote Sensing of Environment, 65(3), 367-375 (1998).

[4] Abrahamson, M. J., Bogdan O. V., Sindiy, O., Biswas, A., "Achieving operational two-way laser acquisition for OPALS payload on the International Space Station," Proc. SPIE 9354 (In Press).

[5] Abhijit Biswas, Bogdan V. Oaida, Kenneth S. Andrews, Joseph M. Kovalik, Matthew J. Abrahamson, and Malcolm W. Wright, "Optical PAyload for Lasercomm Science (OPALS) Link Validation," Proc. SPIE 9354 (In Press).